Optical Pumping of Rubidium

Chidiebube Enwereji
Department of Physics and Astronomy, Dartmouth College
(Dated: June 9, 2026)

We use optical pumping with circularly polarized D_1 light and radio-frequency spectroscopy on a natural-abundance rubidium vapor cell to determine the Landé g-factors of the upper hyperfine ground manifold of each isotope. Linear fits to five resonance measurements per isotope between 150 kHz and 1 MHz give $g_F(^{87}\mathrm{Rb}) = 0.499 \pm 0.011$ and $g_F(^{85}\mathrm{Rb}) = 0.328 \pm 0.007$, both consistent with the theoretical values 1/2 and 1/3 inside the calibration-dominated uncertainty. Their ratio $g_F(^{87}\mathrm{Rb})/g_F(^{85}\mathrm{Rb}) = 1.522 \pm 0.007$, in which the calibration systematic cancels, deviates from the predicted 3/2 by approximately 3σ, indicating a small effect that breaks the isotope-pair symmetry of the measurement. A joint fit of the resonance data yields empirical coil constants consistent with the manufacturer's nominal values to within a few percent. We further observe qualitative evidence for the onset of the quadratic Zeeman regime in ^{87}Rb at fields of order 4 G, and confirm the predicted linear-through-origin scaling of the Rabi frequency with RF drive amplitude in time-resolved transient measurements.

I. INTRODUCTION

Optical pumping exploits the angular momentum carried by circularly polarized photons to drive an atomic vapor far out of thermal equilibrium and concentrate its population in a single magnetic sublevel. The technique, pioneered by Kastler in the 1950s [1], underlies nearly every atomic-physics measurement that begins with a state-prepared sample: atomic clocks, magnetometers, ground-state magnetic-resonance spectroscopy, and the laser-cooled neutral-atom platforms now used for quantum information and precision measurement.

In this experiment we use circularly polarized D_1 light from a rubidium discharge lamp to prepare a vapor of natural-abundance rubidium in the stretched $|F, M = +F\rangle$ state of its upper hyperfine ground manifold, and then interrogate the prepared state with a weak perpendicular radio-frequency field. Resonant absorption between adjacent Zeeman sublevels appears as a dip in the transmitted light intensity, and the field at which that dip occurs as a function of RF frequency directly measures the Landé g-factor of each isotope. The ratio of the two g-factors gives a calibration-independent test of the nuclear-spin assignments $I(^{87}\mathrm{Rb}) = 3/2$ and $I(^{85}\mathrm{Rb}) = 5/2$. A transient version of the same measurement, in which the RF is gated on and off and the resulting Rabi oscillations observed in the time domain, tests the linear scaling of the Rabi frequency with RF amplitude.

II. THEORY AND METHOD

A. Atomic Structure of Rubidium

Rubidium is an alkali metal with a single valence electron outside a closed-shell noble-gas core, making it "hydrogen-like" for the purpose of describing its low-lying energy levels. The ground state places that valence electron in a $5s$ orbital with orbital angular momentum $L = 0$ and spin $S = 1/2$, giving total electronic angular momentum $J = 1/2$. In spectroscopic notation, this is the $5\,^2S_{1/2}$ state. The two lowest excited states arise from promotion to a $5p$ orbital; spin–orbit coupling splits the resulting level into $5\,^2P_{1/2}$ and $5\,^2P_{3/2}$, with the corresponding optical transitions known as the D_1 line at 795 nm and the D_2 line at 780 nm respectively.

Both rubidium isotopes used in this experiment carry a nonzero nuclear spin $\vec{I}$: $I = 3/2$ for ^{87}Rb and $I = 5/2$ for ^{85}Rb. The hyperfine coupling $\hat{H}_{\mathrm{hf}} \propto \hat{\vec{I}} \cdot \hat{\vec{J}}$ between the nucleus and the valence electron means that neither $\vec{J}$ nor $\vec{I}$ is individually conserved, but their sum

$$\vec{F} = \vec{J} + \vec{I} \tag{1}$$

is a constant of the motion. The ground state therefore splits into two hyperfine manifolds labelled by F: $F \in \{1, 2\}$ for ^{87}Rb and $F \in \{2, 3\}$ for ^{85}Rb. In the presence of an external magnetic field $\vec{B}$, each F level further splits via the Zeeman effect into $2F + 1$ magnetic sublevels labelled by the quantum number $M = -F, -F + 1, \ldots, +F$. The structure of these sublevels and the transitions between them are central to everything that follows.

B. Zeeman Splitting and the Resonance Condition

To probe the prepared atomic state—a vapor in which essentially all atoms have been loaded into the single sublevel $M = +F$ by the optical pumping procedure described in Sec. II C—we apply a static magnetic field $\vec{B}$ along the optical axis and an additional small oscillating field perpendicular to it. The interaction of the atomic magnetic moment $\hat{\vec{\mu}}$ with the static field is described by the Zeeman Hamiltonian,

$$\hat{H}_Z = -\hat{\vec{\mu}} \cdot \vec{B}. \tag{2}$$

For an atom in a state with well-defined total angular momentum F, the magnetic moment is proportional to

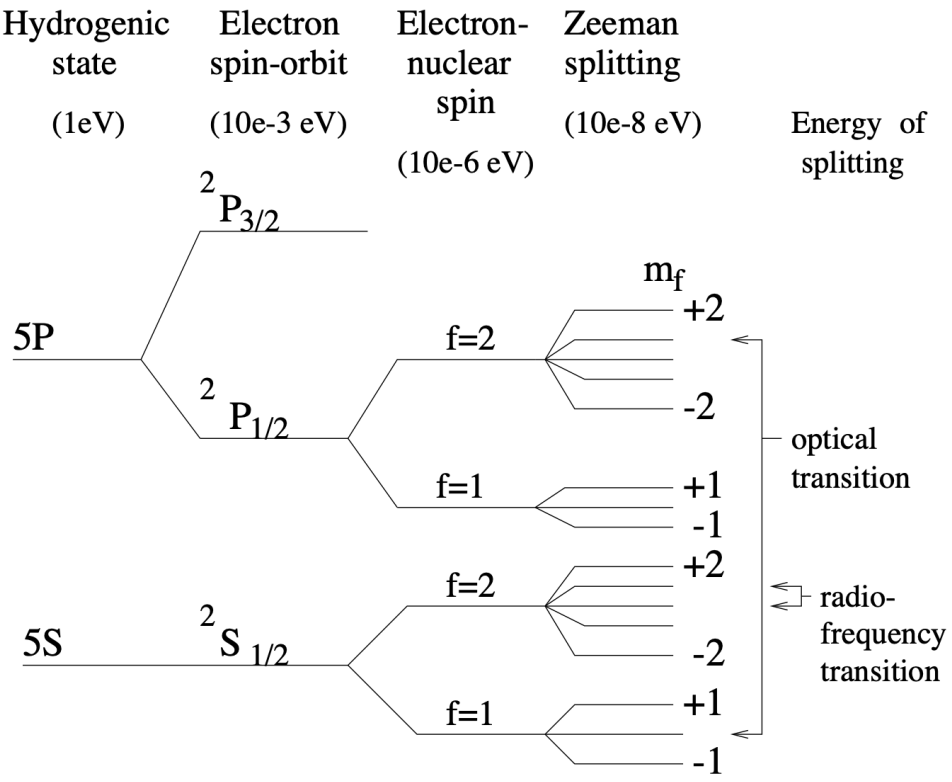

FIG. 1. Energy-level structure of rubidium, showing the successive corrections that produce the levels relevant to this experiment. The bare hydrogenic levels (left, $\sim 1\,\mathrm{eV}$ scale) are refined first by spin–orbit coupling, which splits the $5P$ manifold into the $5\,^2P_{1/2}$ and $5\,^2P_{3/2}$ fine-structure states ($\sim 10^{-3}\,\mathrm{eV}$), then by the hyperfine coupling $\hat{\vec{I}}\cdot\hat{\vec{J}}$, which splits each fine-structure level into manifolds of total angular momentum $F = I \pm J$ ($\sim 10^{-6}\,\mathrm{eV}$). An external magnetic field finally lifts the remaining $(2F+1)$-fold degeneracy by the Zeeman effect ($\sim 10^{-8}\,\mathrm{eV}$). The optical transitions used for pumping drive $5\,^2S_{1/2} \to 5\,^2P_{1/2}$ (the D_1 line), while the RF transitions interrogated in this experiment connect adjacent Zeeman sublevels within $5\,^2S_{1/2}$. Adapted from [2].

$\hat{\vec{F}}$ through the Landé g-factor,

$$\hat{\vec{\mu}} = -g_F\,\mu_B\,\hat{\vec{F}}/\hbar, \tag{3}$$

where $\mu_B = e\hbar/2m_e$ is the Bohr magneton. With $\vec{B} = B\hat{z}$, Eq. 2 becomes $\hat{H}_Z = g_F\mu_B B\,\hat{F}_z/\hbar$, and the eigenstates $|F, M\rangle$ have energies

$$E_M = g_F\,\mu_B\,B\,M. \tag{4}$$

This is a ladder of $2F+1$ equally spaced sublevels with adjacent-level spacing $g_F\mu_B B$. After optical pumping, the entire population sits on the topmost rung, $M = +F$.

The perpendicular oscillating field at frequency ν, produced by a separate set of radio-frequency (RF) coils, resonantly drives transitions between adjacent magnetic sublevels ($\Delta M = \pm 1$) when the RF photon energy matches the Zeeman splitting. Equating $h\nu$ to the spacing in Eq. 4 gives the resonance condition,

$$\nu = \frac{g_F\,\mu_B}{h}\,B. \tag{5}$$

On resonance, the RF redistributes atoms out of the stretched state $|F, +F\rangle$ and across the lower sublevels. Those redistributed atoms are no longer dark to the pumping light—they can once again absorb σ^+ photons, and the transmitted intensity measured at the photodiode *drops*. A dip in transmitted intensity therefore appears whenever the static field B satisfies Eq. 5 for the applied RF frequency. By recording the field at which the dip occurs as a function of ν for each isotope, we directly measure the slope $g_F\mu_B/h$ and extract the Landé factor g_F.

A second, independent mechanism for a dip in the transmitted intensity appears at the opposite limit, $B = 0$. As the static field is reduced toward zero, the Zeeman ladder of Eq. 4 collapses: all $2F+1$ magnetic sublevels become degenerate, and there is no longer a unique quantization axis along which M is even defined. The σ^+ pumping mechanism of Sec. II C cannot establish a coherent population imbalance in the absence of such an axis, so the atoms revert toward a thermal distribution

across the now-degenerate ground manifold and absorption resumes. This produces a "zero-field resonance"—a dip in transmitted intensity centered at $B = 0$ that requires no applied RF to observe. Because its position depends only on the local total magnetic field being zero, it serves as an absolute reference: by recording the sweep-coil current required to null the residual horizontal field, we calibrate the field offset that must be subtracted from every subsequent Zeeman-resonance measurement.

The Landé factor g_F for the upper hyperfine ground state ($F = I + 1/2$) reduces to $g_F = g_J/(2I + 1)$, where $g_J = 2$ for the $5\,^2S_{1/2}$ state (full derivation in [2]). Combined with the nuclear spins $I(^{87}\mathrm{Rb}) = 3/2$ and $I(^{85}\mathrm{Rb}) = 5/2$, this gives theoretical values $g_F(^{87}\mathrm{Rb}) = 1/2$ and $g_F(^{85}\mathrm{Rb}) = 1/3$, and a ratio

$$\frac{g_F(^{87}\mathrm{Rb})}{g_F(^{85}\mathrm{Rb})} = \frac{2I(^{85}\mathrm{Rb}) + 1}{2I(^{87}\mathrm{Rb}) + 1} = \frac{3}{2} \tag{6}$$

that is independent of g_J and serves as a sharp, isotope-pair-specific test of the nuclear spin assignments themselves.

C. Optical Pumping

Optical pumping exploits angular-momentum conservation in the absorption and re-emission of polarized photons. Circularly polarized light (σ^+), carrying one unit of angular momentum, $+\hbar$, along the propagation direction, which we take as the quantization axis $\hat{z}$ incident on an atom forces its magnetic quantum number to increase by one by conservation of angular momentum.

$$\Delta M = +1 \qquad (\text{absorption of } \sigma^+). \tag{7}$$

The excited atom then decays back to the ground manifold by spontaneous emission of an unpolarized photon, and is roughly equally likely to drop with $\Delta M = -1, 0,$ or $+1$. The *average* change in M during a spontaneous decay is therefore zero, while the absorption step strictly raises M by one. Each absorption–emission cycle thus shifts the atom upward on the magnetic ladder by approximately $+1$ on average.

Repeated cycles drive the population to climb until it reaches the topmost sublevel of the upper-hyperfine ground manifold, $M = +F$, the so-called "stretched state." From here, no further σ^+ absorption is possible: the excited-state hyperfine manifolds contain no $M' = F + 1$ sublevel to absorb into, so the selection rule $\Delta M = +1$ has no allowed target. Atoms that reach $M = +F$ are optically dark — they no longer absorb a σ^+ photon. After a characteristic pumping time of order 10 ms, essentially the entire population accumulates in $|F, +F\rangle$ and the cell becomes transparent to the σ^+ light. The transmitted intensity, monitored by a photodiode downstream of the cell, rises sharply as pumping completes. The vapor is now in a single, well-defined quantum state.

III. APPARATUS

The apparatus, shown schematically in Fig. 2, consists of an optical pumping unit with integrated drive and readout electronics, augmented by an external function generator that supplies the RF carrier and an oscilloscope that records the detector signal. Light originates from a rubidium discharge lamp at the upstream end of the optical bench and propagates through a collimating lens, a narrow-bandpass interference filter centered at 795 nm, a linear polarizer, and a quarter-wave plate before entering a rubidium vapor cell located at the geometric center of three orthogonal Helmholtz coil pairs (the static-field assembly) and a smaller perpendicular pair wound on the cell holder (the RF coils). Transmitted light is refocused by a second plano-convex lens onto a silicon photodiode at the downstream end of the bench. The entire optical bench is enclosed in a removable black cloth shroud to suppress stray light and stabilize the local thermal environment.

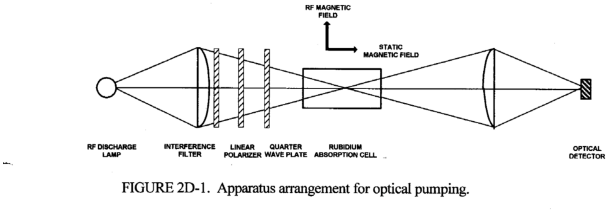

FIGURE 2D-1. Apparatus arrangement for optical pumping.

FIG. 2. Schematic of the optical layout. Light from the RF discharge lamp is collimated, spectrally filtered to the D_1 line, and circularly polarized before entering the rubidium absorption cell. The cell sits inside three orthogonal Helmholtz coil pairs (not all shown) that establish the static magnetic field along the optical axis, and a separate set of RF coils perpendicular to the optical axis. Transmitted light is refocused onto a photodiode. Adapted from [3].

The light source is a sealed bulb containing rubidium metal and a xenon starter gas, held at $\sim$120 °C in a PID-controlled oven and excited by a $\sim$100 MHz RF oscillator. The RF field ionizes the xenon; collisions between the accelerated ions and neutral rubidium atoms excite the rubidium to its $5p$ manifold, and spontaneous decay back to $5\,^2S_{1/2}$ emits the resonance doublet of the D_1 line at 795 nm and the D_2 line at 780 nm. The interference filter immediately downstream of the collimating lens rejects the D_2 component, which is necessary for the pumping mechanism of Sec. II C to operate cleanly: additional decay channels available from $5\,^2P_{3/2}$ would otherwise scramble the angular-momentum bookkeeping that produces the population imbalance. The linear polarizer then selects a single linear polarization from the unpolarized lamp light, and the quarter-wave plate, oriented with its fast axis at 45° to the polarizer's transmission axis, converts that linear polarization to right-circular (σ^+). Each photon emerging from this conditioning stack therefore carries $+\hbar$ of angular momentum along the opti-

cal axis—the resource on which the pumping mechanism depends.

The absorption cell is a sealed Pyrex enclosure containing rubidium vapor in its natural isotopic abundance (72 % ^{85}Rb, 28 % ^{87}Rb) together with 30 torr of neon as a buffer gas, held at $\sim 320\,\mathrm{K}$ in a second PID-controlled oven. The neon suppresses rubidium–wall collisions (which would otherwise depolarize the atoms in tens of microseconds) without itself scrambling the atomic angular momentum, since closed-shell noble gases carry no spin to exchange. Surrounding the cell are three coaxial Helmholtz pairs, of which the largest—the *vertical* pair above and below the cell—cancels the vertical component of the Earth's field. The *main horizontal* pair (154 turns per side, nominal $8.8\,\mathrm{G\,A^{-1}}$) provides the coarse DC field along the optical axis, while a *sweep* pair (11 turns per side, nominal $0.60\,\mathrm{G\,A^{-1}}$) wound directly on top of the main coil provides a finer, electronically rampable contribution along the same axis. Sense resistors ($0.5\,\Omega$ on the main coil, $1\,\Omega$ on the sweep) convert the coil currents to voltages that are available as direct readouts. A much smaller pair of coils wound perpendicular to the optical axis on the cell holder produces the RF magnetic field that drives $\Delta M = \pm 1$ transitions, fed by an integrated amplifier (gain ~ 6, maximum output $\sim 8\,\mathrm{V_{pp}}$) whose output can additionally be gated on and off by an external logic-level signal for the transient measurements of Sec. V E.

After the cell, a second plano-convex lens refocuses the transmitted light onto a silicon photodiode whose photocurrent is converted to a voltage by an on-board transimpedance amplifier, followed by an adjustable-gain stage and a single-pole low-pass filter before reaching the output. A DC-offset stage upstream of the amplifier can subtract the baseline photocurrent, so that the small resonance dips (typically tens of millivolts) are not buried in the several-volt unmodulated photocurrent on which they ride.

IV. SYSTEMATIC UNCERTAINTIES

Two effects that act on the apparatus on every measurement, and that propagate into every quantity reported in Sec. V, deserve characterization before the results themselves are presented. The first, thermal drift, sets a slow time-varying floor on the detector baseline; the second, the ambient magnetic field at the cell, fixes a systematic offset that must be accounted for in every field measurement and that is the dominant contributor to the calibration uncertainty in our extracted Landé factors.

A. Thermal Drift

Both the rubidium discharge lamp and the absorption cell are held at elevated temperatures by independent PID-controlled ovens. The lamp's emitted intensity varies by approximately $5\,\%\,^{\circ}\mathrm{C}^{-1}$ at its operating temperature [3], while the cell's rubidium vapor density rises exponentially with temperature, exponentially modulating the absorption per unit length. The factory-tuned PID parameters have a reset time of $\sim 480\,\mathrm{s}$, so the natural oscillation period of each oven about its setpoint is of order several minutes. The combined effect is a slow modulation of the photodiode baseline on the few-minute timescale, observable directly on the oscilloscope as a trace that drifts upward, levels off, and reverses—inconsistent with simple thermal settling and characteristic instead of underdamped PID hunting.

For the measurements that constitute the bulk of this experiment, thermal drift does *not* shift the location of resonance dips along the magnetic-field axis. Dip positions are set entirely by the Larmor condition $\nu = (g_F \mu_B/h)B$ (Eq. 5), which depends on the magnetic field and the applied RF frequency and is independent of the lamp brightness or cell density. What thermal drift does affect is (i) the absolute DC level of the transmitted intensity, (ii) the depth of each resonance dip, since dip depth is a steady-state response of the pumping kinetics whose rates scale with light intensity and atomic density, and (iii) the precision with which dip centers can be identified on a drifting baseline. The first two effects are minor for our measurements: we extract g_F from dip *positions*, not amplitudes. The third is the only effect that propagates into the uncertainty of our reported quantities, and it does so through the cursor-placement uncertainty on each measured dip.

The apparatus was kept powered continuously across data-acquisition sessions, eliminating any cold-start transient. We observed, however, that changing the sweep-coil Range setting between measurements consistently produced drift behavior qualitatively similar to a cold start: the photodiode baseline would shift and oscillate for tens of seconds to a minute before settling. We attribute this to the change in I^2R dissipation in the sweep coil at the new Range setting perturbing the local thermal environment of the cell and forcing both ovens' PID loops to re-equilibrate. After every Range change we therefore paused for at least one minute before resuming data acquisition. The supplied black cloth was kept draped over the apparatus throughout to stabilize the local thermal environment against drafts and changes in ambient lighting, and the detector DC-offset potentiometer was re-nulled to bring the trace back near zero on the oscilloscope whenever the residual baseline drift moved it out of the high-sensitivity window. With these mitigations in place, the residual baseline drift contributes negligibly to the dip-position uncertainty in the few-second window over which each individual sweep is acquired.

For the transient measurements of Sec. V E, the effect is smaller still: the Rabi periods we measure are of order milliseconds, completely decoupled from the minutes-long thermal oscillations. The lamp's slow brightness drift does scale the overall vertical amplitude of the ringing trace on the oscilloscope, so consecutive Rabi traces

taken at identical RF settings but several minutes apart can show visibly different ringing amplitudes; the zero-crossings of the ringing, from which we extract the period, are unaffected by this scaling.

B. Ambient Magnetic Fields

The absorption cell sits in the unshielded ambient magnetic field of the laboratory, dominated by the Earth's field plus smaller contributions from nearby ferromagnetic material in the building structure and adjacent equipment. The Larmor condition (Eq. 5) involves the *total* magnetic field at the cell, so any uncancelled ambient field along the optical axis adds directly to the field produced by the main and sweep coils and must be subtracted before g_F can be extracted.

The vertical component is cancelled passively by the vertical compensation coil, and the perpendicular horizontal component is cancelled by orienting the entire apparatus along the local Earth field using a compass, leaving only the horizontal component along the optical axis as an unsubtracted offset. We characterize this residual axial field B_{res} by the zero-field-resonance procedure of Sec. II B: the sweep-coil current required to produce a dip in the absence of any applied RF gives B_{res} directly through the calibrated sweep-coil conversion factor. In our setup this yielded $B_{\mathrm{res}} \approx 230\,\mathrm{mG}$, consistent with the local Earth horizontal field to within the calibration tolerances of the coil constants quoted in the manual.

This residual enters every magnetic field measurement reported in Sec. V through the relation

$$B_{\mathrm{net}} = B_{\mathrm{main}} + B_{\mathrm{sweep}} - B_{\mathrm{res}}, \tag{8}$$

so any uncertainty in B_{res} propagates linearly into every individual field measurement. We obtained B_{res} two independent ways and compared them as a consistency check: directly from the zero-field-dip measurement, and from the y-intercept of the linear fit of $B_{\mathrm{main}} + B_{\mathrm{sweep}}$ against ν for each isotope across the five RF frequencies of Sec. V. The three values agreed to within $\sim 5\,\mathrm{mG}$ ($\sim 2\%$), which we adopt as the uncertainty on the residual.

A second, smaller effect of the ambient field is its spatial inhomogeneity over the volume of the cell. The Earth field varies non-negligibly over centimeter scales near building steel, and stray fields from the apparatus's own current-carrying wires add further gradients. This inhomogeneity sets a lower bound on the intrinsic linewidth of any observed resonance, since atoms in different parts of the cell experience slightly different fields and therefore satisfy the Larmor condition at slightly different sweep settings; the manual quotes a typical zero-field-dip FWHM of $\sim 3\,\mathrm{mG}$ for this apparatus [3]. The same broadening sets the floor on how precisely the center of any individual dip can be located with cursors on the oscilloscope trace.

A third effect—time variation of the local ambient field on minutes-to-hours timescales—was checked qualitatively by re-measuring the zero-field dip at the beginning and end of each multi-hour session. The residual shifted by no more than a few mG between such measurements, suggesting that nearby ferromagnetic objects in the lab were not being moved enough during data collection to compromise the calibration.

The dominant systematic in our extracted g_F values is the calibration of the main coil. The TeachSpin manual quotes its nominal main-coil constant as $C_{\mathrm{main}} = 8.8\,\mathrm{G/A}$ but explicitly labels this and the other coil constants as "only approximate", recommending that the student determine more accurate values independently [3]. We did not perform such an independent calibration in this experiment, so our extracted field values inherit whatever error the as-manufactured value carries. For a precision-machined Helmholtz pair with radius $R = 15.79\,\mathrm{cm}$ known to a typical machining tolerance of $\sim 1\,\mathrm{mm}$, the geometric contribution to the field-per-amp uncertainty is $\delta C/C \approx \delta R/R \sim 0.6\,\%$ [4]; allowing for additional contributions from deviations from ideal Helmholtz spacing and finite winding profile, we adopt $\delta C_{\mathrm{main}}/C_{\mathrm{main}} \approx 2\,\%$ as a conservative bound. Combined in quadrature with the explicitly quoted $1\,\%$ sense-resistor tolerance from the manual, the per-point fractional uncertainty in B_{main} is $\delta B/B \approx \sqrt{0.02^2 + 0.01^2} \approx 2.2\,\%$.

This uncertainty is multiplicative and correlated across all measurements—the same coil, the same resistor, and the same multimeter are used throughout—so a multiplicative shift of every B_i by $(1+\varepsilon)$ propagates one-to-one into the slope of the B-vs-ν fit, and therefore into $g_F = h/(m\mu_B)$:

$$\frac{\delta g_F}{g_F} = \frac{\delta m}{m} \approx 2.2\,\%. \tag{9}$$

The residual-field uncertainty of $\sim 5\,\mathrm{mG}$ obtained from the agreement of our two independent B_{res} measurements is, by contrast, an *additive* uncertainty: a constant shift in every B_i moves the intercept of the fit, not its slope. It is therefore absent from Eq. 9, although the fact that the two B_{res} measurements agree within $\sim 2\,\%$ of the residual itself serves as an independent empirical check that the $\sim 2\,\%$ calibration estimate is reasonable. The cursor-placement uncertainty on individual dips—estimated as $\sim 1\,\mathrm{mG}$ per dip based on the $\sim 3\,\mathrm{mG}$ zero-field FWHM quoted by the manual [3]—is uncorrelated between points and contributes only $\sim 0.1\,\%$ to the slope through the standard linear-fit propagation, negligible against the calibration term.

The ratio $g_F(^{87}\mathrm{Rb})/g_F(^{85}\mathrm{Rb})$ is a much tighter test of the underlying physics, because the coil-calibration uncertainty cancels: both isotopes are measured through the same hardware, so any multiplicative error in C_{main} or R_{main} scales both slopes identically and disappears in the ratio.

V. DATA AND ANALYSIS

We begin with the zero-field measurement that fixes the residual ambient field at the cell, follow with the five-frequency low-field Zeeman scans from which we extract Landé g-factors, derive an empirical calibration of the main and sweep coils from the same data, then briefly present qualitative evidence for the onset of the quadratic Zeeman regime, and conclude with the transient Rabi flopping measurements that confirm the predicted linear scaling of the Rabi frequency with RF amplitude.

For every resonance reported below we recorded two voltages at the cursor-defined dip center. The first, V_{main}, is the main-coil sense-resistor voltage read directly off the apparatus front panel with a DMM. The second, V_{rec}, is the sweep-coil recorder output read off the oscilloscope cursor on its x-axis trace: the recorder output is electrically isolated from the main coil, so V_{main} captures everything the main coil is doing and V_{rec} captures everything the sweep coil is doing, with no cross-contamination between them. The two readouts therefore separate cleanly into independent contributions to the total field at the cell.

A. Zero-Field Resonance and Residual Field

With the RF amplifier turned off, we ramped the sweep coil current from zero and identified the position of the photodiode dip that marks the setting at which the total static field along the optical axis crosses zero. A representative trace appears in Fig. 3: as the sweep ramp passes through the cancellation point, the transmitted intensity drops sharply, then recovers as the sweep contribution carries the total field past zero in the opposite sense.

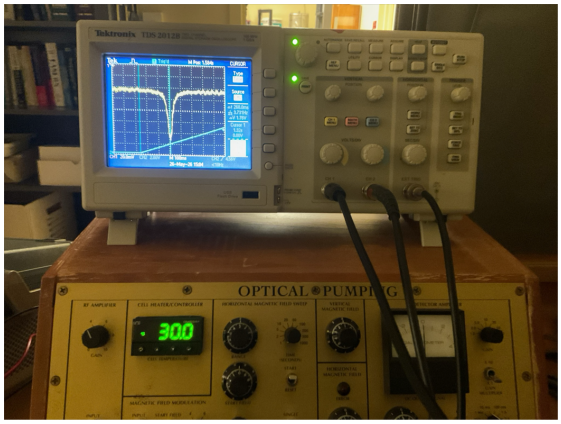

FIG. 3. Oscilloscope trace of the zero-field resonance. With no RF applied, the photodiode signal (yellow) shows a single dip at the sweep value where the total static field at the cell vanishes. The blue trace is the sweep ramp.

At the dip, the total field at the cell is zero, so the sum of the main- and sweep-coil contributions must equal the residual ambient field in magnitude:

$$B_{\mathrm{res}}^{(\mathrm{direct})} = B_{\mathrm{main}} + B_{\mathrm{sweep}}. \tag{10}$$

The main coil carried a small constant offset during the residual measurement of $V_{\mathrm{main}} \approx 12\,\mathrm{mV}$, and the cursor-determined dip occurred at $V_{\mathrm{rec}} \approx 1.76\,\mathrm{V}$. Using the nominal conversions of Sec. III,

$$B_{\mathrm{main}} = V_{\mathrm{main}}\,(\mathrm{mV}) \times 17.6\,\mathrm{mG/mV} \approx 211\,\mathrm{mG},$$
$$B_{\mathrm{sweep}} = V_{\mathrm{rec}}\,(\mathrm{V}) \times 20.0\,\mathrm{mG/V} \approx 35\,\mathrm{mG},$$

giving $B_{\mathrm{res}}^{(\mathrm{direct})} \approx 246\,\mathrm{mG}$. A second, independent determination of B_{res} comes from the y-intercepts of the linear Zeeman fits of Sec. V B below, which yield $B_{\mathrm{res}} = 228.5(61)\,\mathrm{mG}$ from the ^{87}Rb data and $223.0(51)\,\mathrm{mG}$ from the ^{85}Rb data. A third determination from the global joint fit of Sec. V C gives $224(13)\,\mathrm{mG}$. All three values agree to within $\sim 20\,\mathrm{mG}$, with the small spread plausibly attributable to small drifts in the main-coil offset between the time of the direct zero-field measurement and the later Zeeman scans. We adopt the joint-fit value $B_{\mathrm{res}} = 224(13)\,\mathrm{mG}$ as the working number, and use it implicitly through the fit intercepts in everything that follows.

B. Low-Field Zeeman Resonances

For each of five RF frequencies between 150 kHz and 1 MHz, we located the absorption dips of both rubidium isotopes by adjusting the main-coil current to bring each resonance into the sweep window and recording the cursor-defined values of V_{main} and V_{rec} at the dip center. The raw readouts are collected in Table I.

TABLE I. Low-field Zeeman resonance measurements. V_{main} is the front-panel main-coil monitor voltage (DMM, ±1 mV cursor precision) and V_{rec} is the sweep-coil recorder output read from the oscilloscope x-axis at the dip center (±0.05 V cursor precision).

ν (kHz)	Isotope	V_{main} (mV)	V_{rec} (V)
150	^{87}Rb	15	9.06
150	^{85}Rb	19	10.7
200	^{87}Rb	20	8.28
200	^{85}Rb	24	11.8
400	^{87}Rb	31	12.6
400	^{85}Rb	47	13.4
600	^{87}Rb	52	8.38
600	^{85}Rb	76	9.70
1000	^{87}Rb	82	11.0
1000	^{85}Rb	125	10.0

Combining the two contributions using the nominal calibration factors gives the total applied field $B_{\mathrm{tot}} = B_{\mathrm{main}} + B_{\mathrm{sweep}}$ at each resonance. Figure 4 plots B_{tot} against ν for both isotopes. Error bars represent the

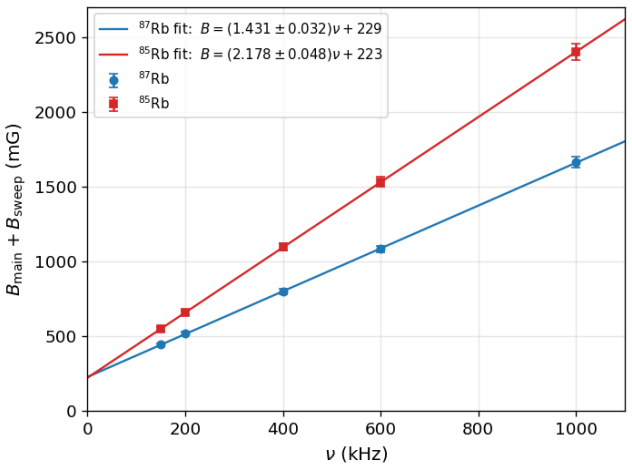

FIG. 4. Total coil-applied field $B_{\mathrm{main}} + B_{\mathrm{sweep}}$ versus RF frequency ν for both rubidium isotopes. Solid lines are linear least-squares fits; their slopes give the Landé g-factors via Eq. 13 and their y-intercepts give the residual ambient field along the optical axis.

2.2 % calibration uncertainty propagated to each point (Sec. IV B).

Linear least-squares fits to the two data sets give

$$m(^{87}\mathrm{Rb}) = 1.431(32)\,\mathrm{mG/kHz}, \qquad c(^{87}\mathrm{Rb}) = 228.5(61)\,\mathrm{mG}, \tag{11}$$

$$m(^{85}\mathrm{Rb}) = 2.178(48)\,\mathrm{mG/kHz}, \qquad c(^{85}\mathrm{Rb}) = 223.0(51)\,\mathrm{mG}, \tag{12}$$

where the quoted slope uncertainties combine the statistical (polyfit-residual) and systematic (calibration) contributions in quadrature. The Landé factors follow from the resonance condition (Eq. 5) rearranged as

$$g_F = \frac{h}{m\,\mu_B} = \frac{1}{m \cdot (\mu_B/h)}, \tag{13}$$

giving

$$g_F(^{87}\mathrm{Rb}) = 0.499 \pm 0.011, \qquad g_F(^{85}\mathrm{Rb}) = 0.328 \pm 0.007, \tag{14}$$

both consistent with the theoretical values 1/2 and 1/3 inside the calibration-dominated uncertainty.

The ratio of measured slopes,

$$\frac{g_F^{\mathrm{meas}}(^{87}\mathrm{Rb})}{g_F^{\mathrm{meas}}(^{85}\mathrm{Rb})} = \frac{m(^{85}\mathrm{Rb})}{m(^{87}\mathrm{Rb})} = 1.522 \pm 0.007, \tag{15}$$

deviates from the theoretical 3/2 by 1.5 %, or roughly 3σ under the uncorrelated portion of the slope uncertainty alone (the calibration cancels in this ratio, as discussed in Sec. IV B, leaving only the polyfit-residual contribution). The deviation is real at the few-sigma level given the propagated statistics, and points to an effect that acts asymmetrically on the two isotope slopes; candidate mechanisms were discussed in Sec. IV B.

C. Empirical Coil Calibration

The manual labels the coil constants of Table I as "only approximate" (Sec. IV B) [3], and an empirical determination is possible from the same data once theoretical g_F values are assumed. Each resonance must satisfy

$$\frac{h\,\nu_i}{g_F^{(i)}\,\mu_B} = a\,V_{\mathrm{main},i} + b\,V_{\mathrm{rec},i} + c, \tag{16}$$

where a and b are the empirical conversion factors (in mG/mV and mG/V) and $c = -B_{\mathrm{res}}$. Performing a joint three-parameter linear least-squares fit on all ten data points yields

$$a = 17.37(6)\,\mathrm{mG/mV}, \quad b = 20.0(12)\,\mathrm{mG/V}, \quad c = -224(13)\,\mathrm{mG}. \tag{17}$$

Converted back to physical coil constants, this gives

$$C_{\mathrm{main}} = 8.685(29)\,\mathrm{G/A}, \qquad (\text{manual nominal } 8.80\,\mathrm{G/A}) \tag{18}$$

$$C_{\mathrm{sweep}} = 0.601(36)\,\mathrm{G/A}, \qquad (\text{manual nominal } 0.60\,\mathrm{G/A}). \tag{19}$$

The main-coil constant differs from the manual's nominal by 1.3 % while the sweep-coil constant is consistent with nominal to better than 1 %. The empirical residual $B_{\mathrm{res}} = 224(13)\,\mathrm{mG}$ agrees with both the direct zero-field measurement of Sec. V A and the individual-isotope fit intercepts of Sec. V B.

Figures 5 and 6 display the joint calibration in the two-plot form used by the manual. In each plot, the contribution of one coil is subtracted off the resonance-implied total field (the left-hand side of Eq. 16) using the joint-fit value of the other coil's empirical constant, so that the remaining y value is the contribution of the plotted coil alone.

Because both isotopes' data enter the joint fit with their theoretical g_F values held fixed, this calibration is a self-consistency check rather than an independent test of the g_F theory. It does, however, establish that the manual's nominal coil constants are accurate for our particular unit at the level of a few percent, and pin down B_{res} to $\pm 13\,\mathrm{mG}$ from data taken on the same morning as the rest of the experiment.

D. Onset of the Quadratic Zeeman Effect

To search for the onset of the quadratic Zeeman regime—where the $2F+1$ magnetic sublevels of a hyperfine manifold no longer maintain exactly uniform spacing and the single resonance line of Sec. V B splits into $2F$ distinct transitions—we raised the main-coil current to $\sim 0.5\,\mathrm{A}$ ($B_{\mathrm{main}} \approx 4.4\,\mathrm{G}$) and rescanned the sweep at an RF frequency of 3 MHz. Within a sweep window of $\sim 60\,\mathrm{mG}$ centered on the ^{87}Rb resonance we resolved a

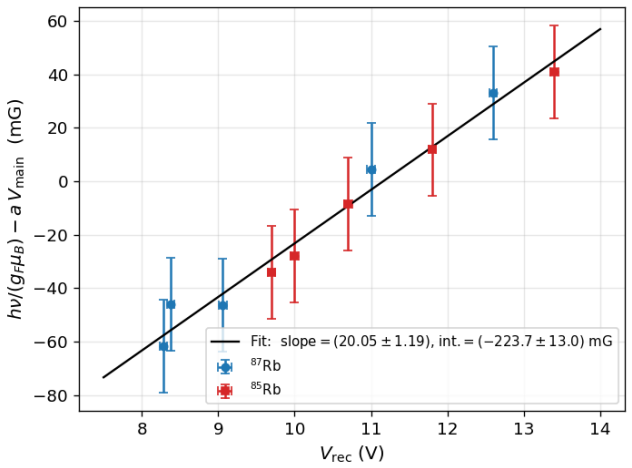

FIG. 5. Empirical calibration of the sweep coil. The plotted y value is the resonance-implied total field minus the main-coil contribution (using the joint-fit value of a), leaving the sweep-coil contribution alone, plotted against V_{rec}. The slope is the empirical conversion factor b, and the intercept gives $-B_{\mathrm{res}}$.

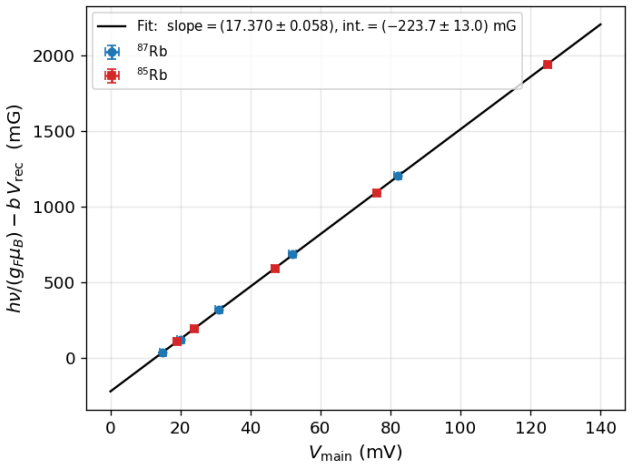

FIG. 6. Empirical calibration of the main coil, in the same form as Fig. 5 with the roles of the two coils exchanged. The slope gives the empirical a, and the intercept gives $-B_{\mathrm{res}}$. The cleaner alignment of the data with the fit line here, compared to Fig. 5, reflects the much larger lever arm V_{main} provides across the dataset.

partially-distinct multiplet of three to four closely spaced dips (Fig. 7).

The presence of multiple resolved dips inside what was previously a single resonance line is a qualitative confirmation of the quadratic correction to the linear Zeeman ladder of Eq. 4, consistent with the predicted onset of sublevel-resolved structure for ^{87}Rb $F = 2$ at fields of a few gauss. We did not pursue a quantitative fit to the individual sublevel splittings.

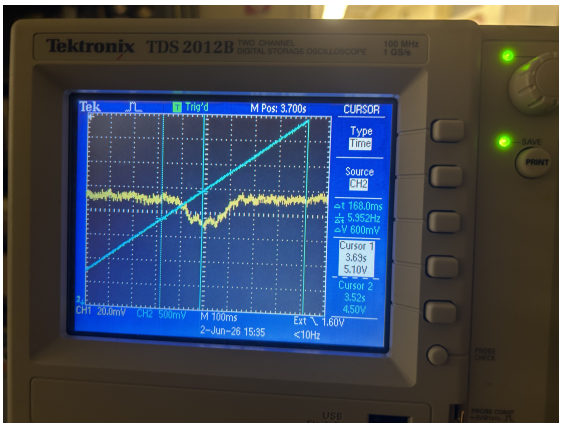

FIG. 7. Oscilloscope trace of the ^{87}Rb resonance at $\nu = 3\,\mathrm{MHz}$ and $B_{\mathrm{main}} \approx 4.4\,\mathrm{G}$, showing the partially-resolved quadratic Zeeman multiplet. Cursors at $V_{\mathrm{rec}} = 4.50\,\mathrm{V}$ and $5.10\,\mathrm{V}$ ($\Delta V = 600\,\mathrm{mV}$, $\Delta B \approx 12\,\mathrm{mG}$) bracket the visible multiplet structure.

E. Rabi Flopping

To test the prediction that the Rabi frequency scales linearly with the amplitude of the perpendicular RF drive, $\Omega_R = g_F \mu_B B_{\mathrm{RF}}/\hbar$, we parked the static field on the ^{87}Rb resonance at an RF carrier frequency of 50 kHz and gated the RF on and off with a $\sim 1\,\mathrm{Hz}$ TTL square wave applied to the modulation input. The oscilloscope was triggered on the falling edge of the gate in storage mode. After each RF turn-on, the detector signal showed a clean damped sinusoid with the underdamped envelope decaying over several oscillation periods. A representative trace at $V_{\mathrm{pp}} = 1.00\,\mathrm{V}$ is shown in Fig. 8.

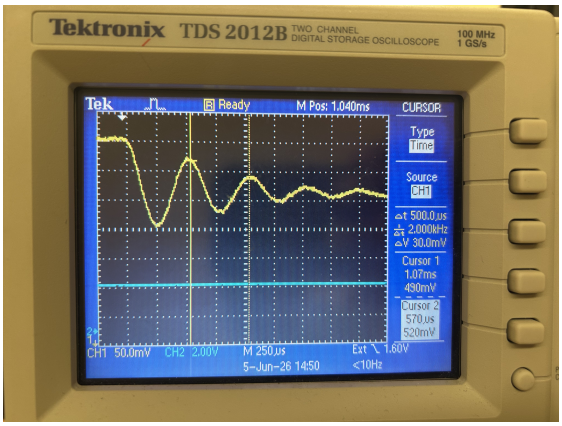

FIG. 8. Oscilloscope trace of the Rabi ringing at $V_{\mathrm{pp}} = 1.00\,\mathrm{V}$, time base $250\,\mu\mathrm{s/div}$. Cursors at $\Delta t = 500\,\mu\mathrm{s}$ measure the period T; the corresponding Rabi frequency is $f_R = 1/T = 2000\,\mathrm{Hz}$.

We measured the Rabi period $T = 2\pi/\Omega_R$ by placing cursors at successive zero-crossings of the ringing at four function-generator amplitudes V_{pp} between 0.25 V and 1.0 V. Table II collects the measurements; Fig. 9 plots

the period against $V_{\rm pp}$ in the form used by the manual.

TABLE II. Rabi flopping measurements on the ^{87}Rb resonance at 50 kHz. Period T is measured between successive zero-crossings of the detector ringing with a cursor precision of $\sim$20 µs.

$V_{\rm pp}$ (V)	T (μs)	$f_R = 1/T$ (Hz)
0.25	1880	532
0.50	1080	926
0.75	640	1563
1.00	500	2000

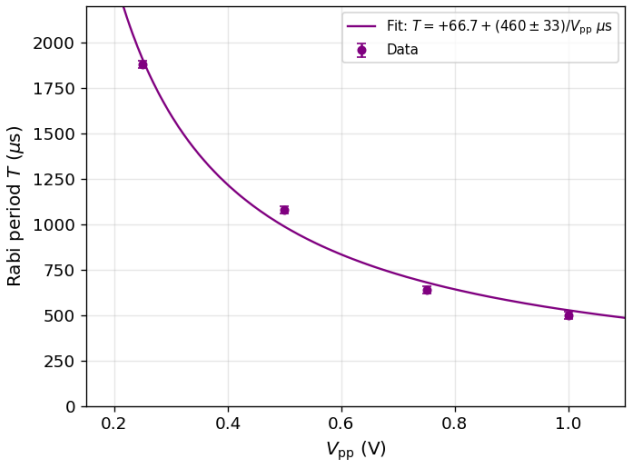

FIG. 9. Rabi period T on the ^{87}Rb resonance versus the function-generator amplitude $V_{\rm pp}$, with hyperbolic fit $T = T_0 + k/V_{\rm pp}$. Error bars reflect the ±20 µs cursor precision on each period measurement.

A least-squares fit to the form $T = T_0 + k/V_{\rm pp}$ used in the manual gives

$$T = (67(79)\,\mu\text{s}) + \frac{460(33)\,\mu\text{s}\cdot\text{V}}{V_{\rm pp}}, \tag{20}$$

with the constant term T_0 consistent with zero on the scale of the slope. Equivalently, the Rabi frequency varies linearly with $V_{\rm pp}$,

$$f_R = (2016(128)\,\text{Hz/V})\,V_{\rm pp} + (-5(88)\,\text{Hz}), \tag{21}$$

again with an intercept consistent with zero. The actual content of the test is the through-origin linearity: a finite intercept in either form would signal a non-RF mechanism setting the oscillation rate (e.g. a stray DC field component coupling to $g_F\mu_B/\hbar$), while the observed linear-through-origin relationship is exactly the prediction of the Rabi formula with the RF coil treated as a linear transducer between drive voltage and applied field. The slope 2016(128) Hz/V establishes the empirical proportionality between function-generator amplitude and Rabi frequency at the cell, combining the gain of the RF amplifier, the geometric coupling of the RF coil to the cell, and the rotating-wave projection of the linearly polarized drive onto the resonant circular component.

A complementary prediction—that the slope of f_R vs $V_{\rm pp}$ for ^{85}Rb at the same drive should differ from the ^{87}Rb slope by the inverse of the g-factor ratio of Eq. 15—could in principle be tested by repeating the amplitude sweep on the ^{85}Rb resonance, but was not pursued.

VI. CONCLUSION

We have used optical pumping and Zeeman-resonance spectroscopy to determine the Landé g-factors of the upper hyperfine ground manifold of both rubidium isotopes. The extracted values, $g_F(^{87}\text{Rb}) = 0.499 \pm 0.011$ and $g_F(^{85}\text{Rb}) = 0.328 \pm 0.007$, agree with the theoretical predictions 1/2 and 1/3 within the $\sim 2.2\,\%$ calibration-dominated systematic uncertainty. Their ratio $g_F(^{87}\text{Rb})/g_F(^{85}\text{Rb}) = 1.522 \pm 0.007$, in which the calibration cancels because both isotopes are measured through the same hardware, deviates from the predicted 3/2 by approximately 3σ under the propagated polyfit-residual uncertainty alone. The deviation cannot be explained by the systematics characterized in Sec. IV; it points to an effect acting asymmetrically on the two isotopes' slopes, with plausible candidates including lineshape distortion from the early onset of quadratic Zeeman broadening, unequal pumping kinetics on the $F = 2$ and $F = 3$ ground manifolds, and a per-dip cursor uncertainty estimated too low.

A joint fit of the resonance data yields empirical coil constants $C_{\rm main} = 8.685(29)\,\text{G/A}$ and $C_{\rm sweep} = 0.601(36)\,\text{G/A}$, consistent with the manufacturer's nominal specifications at the percent level, and pins down the residual ambient field along the optical axis to $B_{\rm res} = 224(13)\,\text{mG}$ in agreement with the direct zero-field measurement. We qualitatively observe the onset of the quadratic Zeeman regime in ^{87}Rb at $B \approx 4.4\,\text{G}$, and the transient Rabi-flopping measurement confirms the predicted linear-through-origin scaling of the Rabi frequency with the perpendicular RF drive amplitude.

The principal limitation of this experiment is the absence of an independent calibration of the static-field coils. The manual labels its quoted coil constants as approximate and recommends an external measurement, which we did not perform; the per-isotope g_F values therefore inherit a few-percent systematic that the ratio test partially circumvents but cannot eliminate. A Hall-probe or NMR characterization of $C_{\rm main}$ and $C_{\rm sweep}$ would convert the present percent-level result into a precision absolute determination of g_F for each isotope, and would be the natural next step in extending this experiment.

[1] A. Kastler, Journal de Physique et le Radium **11**, 255 (1950).

[2] MIT Department of Physics, *Optical Pumping*, Junior Lab experiment writeup Experiment 11 (Massachusetts Institute of Technology, 2011) `https://web.mit.edu/8.13/www/JLExperiments/JLExp11.pdf`.

[3] *Optical Pumping of Rubidium: Instructor's Manual*, TeachSpin, Inc., Buffalo, NY, model OP1-A.

[4] D. J. Griffiths, *Introduction to Electrodynamics*, 4th ed. (Cambridge University Press, 2017).